

# **GROUND OPTICAL SIGNAL PROCESSING ARCHITECTURE FOR CONTRIBUTING SPACE-BASED SSA SENSOR DATA**

**Darin Koblick, Alfred Goldsmith, Michael Klug, and Pete Mangus**

*Millennium Space Systems, Inc. El Segundo, CA.*

**Brien Flewelling, and Moriba Jah**

*Air Force Research Laboratory, Albuquerque, NM.*

**Joe Shanks, and Robert Piña**

*Raytheon/Photon Research Associates. San Diego, CA.*

**Jason Stauch, and Jason Baldwin**

*Schafer Corporation, Albuquerque, NM.*

**James Campbell**

*CENTRA Technology, Arlington, VA.*

**Lt Col Travis Blake, PhD, USAF**

*Defense Advanced Research Projects Agency, Arlington, VA.*

## **ABSTRACT**

DARPA's OrbitOutlook aims to augment the performance of the Space Surveillance Network's Space Situational Awareness (SSA) by adding more data more often from more diverse sources to increase Space Domain Awareness (SDA) and determine when satellites are at risk. OrbitOutlook also seeks to demonstrate the ability to rapidly include new instruments to alert for indications and warnings of space events. [1] In order to accomplish this, an underlying framework to process sensor data and provide useful products, such as angles-only measurements, is required. While existing optical signal processing implementations are capable of converting raw sensor data to angles-only measurements, they may be difficult to customize, obtain, and deploy on low-cost demonstration programs. The Ground Optical Signal Processing Architecture (GOSPA) (inexpensive, easy to customize, obtain, and deploy) can ingest raw imagery and telemetry from a space-based optical sensor and perform a background subtraction process to remove anomalous pixels, interpolate over bad pixels, and dominant temporal noise. Streak end points and target centroids are located using the AFRL Generalized Electro-Optical Detection, Tracking, ID, and Characterization Application (GEODETICA); an image data reduction pipeline for ground and space-based SSA. These identified streak locations are fused with the corresponding telemetry to determine the Right Ascension and Declination (RA/DEC) measurements. The measurements are processed through the AFRL Constrained Admissible Region Multiple Hypothesis Filter (CAR-MHF) to determine its initial orbit (IOD). GOSPA performance is demonstrated using non-rate tracking collections against a satellite in GEO, simulated from a visible optical imaging sensor in a polar LEO. Stars, noise and bad pixels are simulated based on look angles and sensor parameters. Under this scenario, GOSPA generated an IOD with absolute position/velocity errors of less than 2.5 km and 0.3 m/s using sensor RA/DEC RSS pointing uncertainties as large as 70.7 arcsec. This demonstrates the capability for GOSPA to support contributing SSA space-based optical sensors under OrbitOutlook and subsequently provide useful data back to space command and control.

## **1. INTRODUCTION**

OrbitOutlook ( $O^2$ ) is a DARPA sponsored program with the objective of augmenting the Space Surveillance Network (SSN) by adding contributing optical and radar sensors with diverse geographic locations. [1] This includes space-based as well as ground-based measurement collection capabilities. While SpaceView exists to provide a mechanism to allow for  $O^2$  to remotely control ground telescopes, a cost effective rapidly deployable signal processing architecture has not been identified or socialized within the SSA community to allow for the performance prediction modeling and real-time operational processing of Resident Space Object (RSO)/target collections using contributing space-based optical sensors.

While contributing SSA ground-based optical sensor collectors have a low cost of acquisition, most systems are sensitive to the background sky brightness and are relegated to night time operation. Space-based optical sensors, with lower Sun and Earth exclusion limits can help to eliminate this daytime collection gap imposed by ground-based optical systems and are therefore critical to achieving better response and warning times to space events. Studies from the Space-Based Visible program indicate that with the use of efficient search patterns, it is possible

Report Documentation Page		Form Approved OMB No. 0704-0188
Public reporting burden for the collection of information is estimated to average 1 hour per response, including the time for reviewing instructions, searching existing data sources, gathering and maintaining the data needed, and completing and reviewing the collection of information. Send comments regarding this burden estimate or any other aspect of this collection of information, including suggestions for reducing this burden, to Washington Headquarters Services, Directorate for Information Operations and Reports, 1215 Jefferson Davis Highway, Suite 1204, Arlington VA 22202-4302. Respondents should be aware that notwithstanding any other provision of law, no person shall be subject to a penalty for failing to comply with a collection of information if it does not display a currently valid OMB control number.		
1. REPORT DATE <b>SEP 2014</b>	2. REPORT TYPE	3. DATES COVERED <b>00-00-2014 to 00-00-2014</b>
4. TITLE AND SUBTITLE <b>Ground Optical Signal Processing Architecture for Contributing Space-based SSA Sensor Data</b>		5a. CONTRACT NUMBER
		5b. GRANT NUMBER
		5c. PROGRAM ELEMENT NUMBER
6. AUTHOR(S)	5d. PROJECT NUMBER	
	5e. TASK NUMBER	
	5f. WORK UNIT NUMBER	
7. PERFORMING ORGANIZATION NAME(S) AND ADDRESS(ES) <b>Air Force Research Laboratory, Kirtland AFB, NM, 87117</b>		8. PERFORMING ORGANIZATION REPORT NUMBER
9. SPONSORING/MONITORING AGENCY NAME(S) AND ADDRESS(ES)		10. SPONSOR/MONITOR'S ACRONYM(S)
		11. SPONSOR/MONITOR'S REPORT NUMBER(S)
12. DISTRIBUTION/AVAILABILITY STATEMENT <b>Approved for public release; distribution unlimited</b>		
13. SUPPLEMENTARY NOTES <b>In the Advanced Maui Optical and Space Surveillance Technologies (AMOS) Conference, 9-12 Sep 2014, Maui, HI.</b>		

## 14. ABSTRACT

**DARPA's OrbitOutlook aims to augment the performance of the Space Surveillance Network's Space Situational Awareness (SSA) by adding more data more often from more diverse sources to increase Space Domain Awareness (SDA) and determine when satellites are at risk. OrbitOutlook also seeks to demonstrate the ability to rapidly include new instruments to alert for indications and warnings of space events. [1] In order to accomplish this, an underlying framework to process sensor data and provide useful products, such as angles-only measurements, is required. While existing optical signal processing implementations are capable of converting raw sensor data to angles-only measurements, they may be difficult to customize, obtain, and deploy on low-cost demonstration programs. The Ground Optical Signal Processing Architecture (GOSPA) (inexpensive, easy to customize, obtain, and deploy) can ingest raw imagery and telemetry from a space-based optical sensor and perform a background subtraction process to remove anomalous pixels, interpolate over bad pixels, and dominant temporal noise. Streak end points and target centroids are located using the AFRL Generalized Electro-Optical Detection, Tracking, ID, and Characterization Application (GEODETICA); an image data reduction pipeline for ground and space-based SSA. These identified streak locations are fused with the corresponding telemetry to determine the Right Ascension and Declination (RA/DEC) measurements. The measurements are processed through the AFRL Constrained Admissible Region Multiple Hypothesis Filter (CAR-MHF) to determine its initial orbit (IOD). GOSPA performance is demonstrated using non-rate tracking collections against a satellite in GEO, simulated from a visible optical imaging sensor in a polar LEO. Stars, noise and bad pixels are simulated based on look angles and sensor parameters. Under this scenario, GOSPA generated an IOD with absolute position/velocity errors of less than 2.5 km and 0.3 m/s using sensor RA/DEC RSS pointing uncertainties as large as 70.7 arcsec. This demonstrates the capability for GOSPA to support contributing SSA space-based optical sensors under OrbitOutlook and subsequently provide useful data back to space command and control.**

## 15. SUBJECT TERMS

## 16. SECURITY CLASSIFICATION OF:

a. REPORT

**unclassified**

b. ABSTRACT

**unclassified**

c. THIS PAGE

**unclassified**17. LIMITATION OF  
ABSTRACT**Same as  
Report (SAR)**18. NUMBER  
OF PAGES**11**19a. NAME OF  
RESPONSIBLE PERSON

for contributing SSA sensors (especially slew rate limited payloads) to cover most of the GEO belt within six hours. [3] Subsequently, with the enhanced SSA collection capabilities offered by O<sup>2</sup>, the space command and control would not be able to process the increased amount of data that could be delivered and it could not be readily used.[2] In order to obtain useful information from an optical sensor collection, the target must be distinguished from noise and other signal sources (e.g. stars, planets, and other space objects). This type of processing involves detailed knowledge of the optical detector as well as the tracking CONOPS, platform position and orientation during the collection period, and the ability to associate objects obtained from separate observations. The Millennium Space Systems led Ground Optical Signal Processing Architecture (GOSPA) addresses the current need for a low-cost Space Situational Awareness (SSA) processing architecture solution in support of DARPA TTO's O<sup>2</sup> program to include systems that were not originally designed to contribute SSA but are technically capable. Fig 1 summarizes the physics based simulation which was developed for the verification and validation of the GOSPA process.

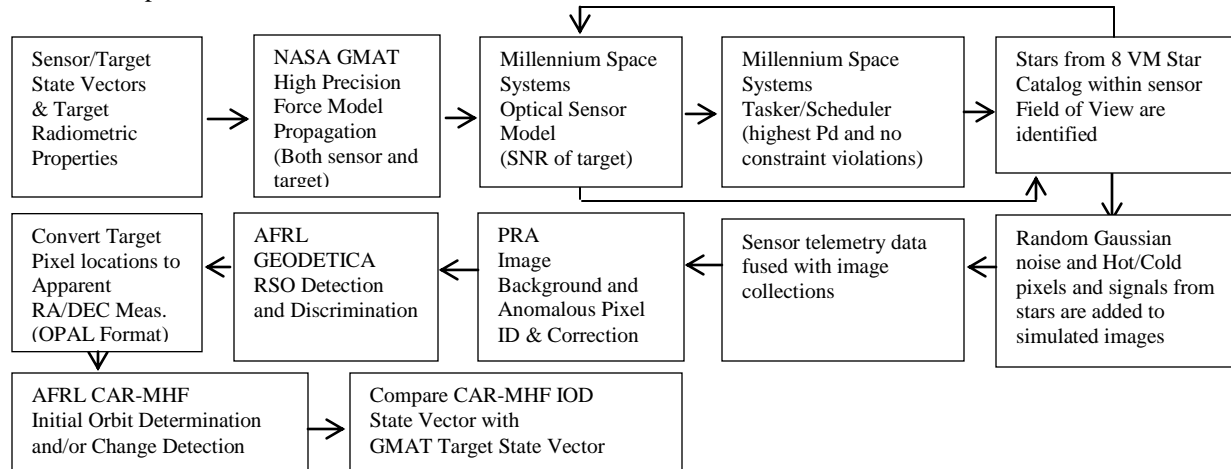


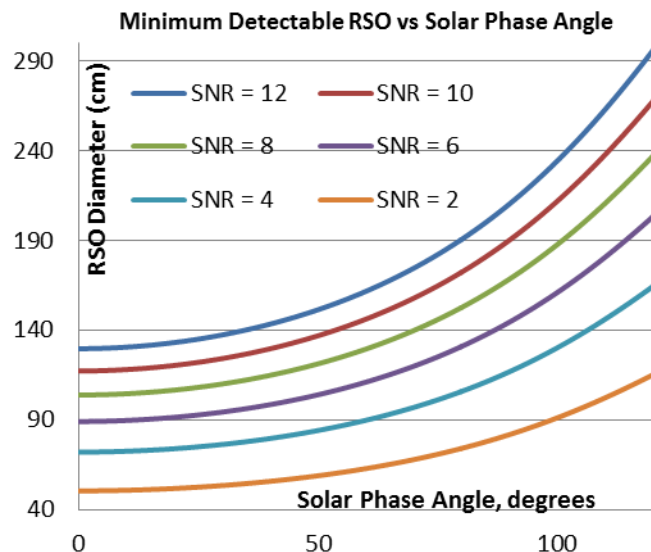
Fig 1: Physics Based Optical Models and High-Precision Orbit Propagation Integrated into the GOSPA Simulation

## 2. SPACE-BASED OPTICAL SENSOR MODEL

A hypothetical contributing SSA sensor using a generic representation of a body fixed space-based sensor is proposed [3]. The optical parameters and sensor properties used in the Signal to Noise Ratio (SNR) model are provided in Table 1.

Table 1: Optical Sensor Modeling Parameters with accompanying graph of sensor performance for a space-based LEO sensor observing a GEO object assuming a relative angular rate of 30 arcsec.

Focal Plane Array Size	512 x 512 pixels
Pixel Size (Length x Width)	20 $\mu$ m x 20 $\mu$ m
Well Capacity (electrons)	170,000
Digital Quantization (A/D bits)	12 bits
Quantum Efficiency	80%
Optical Throughput	0.80
Integration Time	1 sec
Spectral Range	0.300 – 0.900 $\mu$ m
Sensor Field of View	1.0 x 1.0 deg
Frame Stacking	1 Co-added Frames
Aperture Diameter	15 cm
Aperture Area Obscuration	0.10
Number of Frames per Frameset	8 Frames
Instantaneous Field of View	7.04 arcsec/pixel
Energy on Detector (EOD)	0.70
Read Noise	50 electrons
Pixel Area Fill Factor	1
Gain	12
Reset or Calibration Time	20 seconds
Multiplexer Voltage (full swing)	2 volts
Dark Current	7E-18 Amps
Dark Current/Responsivity Non-Uniformity	0.00002 Fraction
Background Visual Magnitude	22 Mv/arcsec <sup>2</sup>
Probability of False Alarm (Pfa)	1E-4



The configuration of the optical sensor model is illustrated in Fig 2.

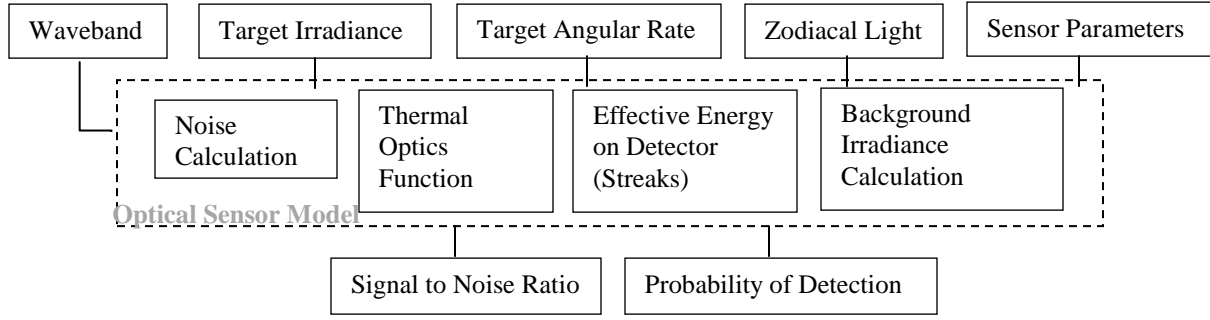


Fig 2: Optical Sensor Model

The sensor model has the capability of converting visual magnitudes to radiometric quantities. However, since the model covers the full range of light (from UV through VLWIR) a more generic description of this model is provided. An optical signal, due to a point source or streak, is given by (1)

$$\text{signal} = \Phi_{\text{tot}} \cdot A_{\text{optics}} \cdot \eta_{\text{optics}}^N \cdot \text{EOD}_{\text{effective}} \cdot \text{QE} \cdot t_{\text{int}} \quad (1)$$

Where  $\Phi_{\text{tot}}$  is the total photon flux of the target at the aperture of the optical system,  $A_{\text{optics}}$  is the aperture area.

$\eta_{\text{optics}}$  is the average optical transmission per optical element,  $N$ .  $\text{EOD}_{\text{effective}}$  is the effective energy on detector for a streaked or stationary target, QE is the in-band quantum efficiency, and  $t_{\text{int}}$  is the integration time of each frame. The signal to noise ratio, SNR, is given by (2)

$$\text{SNR} = \frac{\text{signal}}{\text{noise}} \sqrt{N_{\text{coadds}}} \quad (2)$$

Where  $N_{\text{coadds}}$  is either the number of frame co-adds or time delay integrations. The noise is given by (3)[4][5]:

$$\text{noise} = \sqrt{\text{dN}_{\text{photons}}^2 + \text{dN}_{\text{photonsFPN}}^2 + \text{dN}_{\text{drk}}^2 + \text{dN}_{\text{drkFPN}}^2 + \text{dN}_j^2 + \text{dN}_{\text{read}}^2 + \text{dN}_{\text{d1f}}^2 + \text{dN}_{\text{ktc}}^2 + \text{dN}_{\text{v1f}}^2 + \text{dN}_{\text{aw}}^2 + \text{dN}_{\text{a2d}}^2} \quad (3)$$

Where  $\text{dN}_{\text{photons}} = \sqrt{\text{signal} + \text{dN}_{\text{thermal}}^2 + \text{dN}_{\text{zodiacal}}^2}$  and  $\text{dN}_{\text{read}}$  is the read noise in noise-electrons.  $\text{dN}_{\text{thermal}}$  is the photoelectron noise due to the temperature of the focal plane.  $\text{dN}_{\text{zodiacal}}$  is the photoelectrons due to background light.  $\text{dN}_{\text{photonFPN}}$  is the sensor responsivity fixed pattern noise.  $\text{dN}_{\text{drk}}$  is the detector dark current noise.  $\text{dN}_{\text{drkFPN}}$  is the detector dark current non-uniformity.  $\text{dN}_j$  is the Johnson and Shunt Noise.  $\text{dN}_{\text{d1f}}$  is the detector 1/f noise. [6]  $\text{dN}_{\text{ktc}}$  is the capacitance switching noise.  $\text{dN}_{\text{v1f}}$  is the amplifier input referred 1/f noise. [5]  $\text{dN}_{\text{aw}}$  is the amplifier input referred white noise, and  $\text{dN}_{\text{a2d}}$  is the digitization noise. Note that unless otherwise specified, the units of all individual noise terms are in electrons or noise-electrons. Other functions include an approximation for the resistance-area product,  $R_oA$ , vs detector cutoff wavelength, the effective EOD, and the formulas for the various radiometric/photometric quantities.

### 3. ORBIT PROPAGATION FORCE MODEL

The General Mission Analysis Tool (GMAT), developed by the Goddard Space Flight Center at NASA, was chosen to perform the orbit propagation of both the target satellites and the sensor platform. For this analysis, it is assumed that the targets and the sensor are not maneuvering during the simulation period. The second order differential equation to describe the motion of a satellite is provided (4) [7]:

$$\frac{d^2 \mathbf{r}}{dt^2} = \sum \frac{\mathbf{F}_{\text{ext}}}{m} = -\frac{\mu}{r^3} \bar{\mathbf{r}} + \nabla \phi_{sj}^\circ + G \sum_{\substack{k=1 \\ k \neq j}}^{n_b} m_k \left( \frac{r_{ks}}{r_{ks}^3} - \frac{r_{kj}}{r_{kj}^3} \right) + \frac{P_{SR} C_R A_\Theta}{m_s} \hat{\mathbf{r}}_{s\Theta} \quad (4)$$

Where  $-\frac{\mu}{r^3}\bar{r}$  describes the central body point mass,  $\nabla\phi_{sj}^\circ$  is the central body direct non-spherical force component,

$G\sum_{\substack{k=1 \\ k \neq j}}^{n_b} m_k \left( \frac{r_{ks}}{r_{ks}^3} - \frac{r_{kj}}{r_{kj}^3} \right)$  is the direct and indirect third body point mass, and  $\frac{P_{SR}C_R A_\Theta}{m_s} \hat{r}_{s\Theta}$  describes the solar radiation

pressure.

For simulation purposes, the following force model parameters and models were chosen for the propagation of both sensor and target satellites:

Table 2: General Mission Analysis Tool Force Model Settings for All Satellites

Central Body Point Mass	Earth
Third Body Point Mass	Sun, Mercury, Venus, Moon, Mars, Jupiter, Saturn, Uranus, Neptune, and Pluto
Earth Gravity Model	Earth Gravity Model 1996
Gravity Field Degree and Order	100 x 100
Spacecraft Coefficient of Reflectivity (C <sub>R</sub> )	0.7
f107Average (81-day averaged 10.7cm solar flux)	150
F107daily (Daily 10.7cm solar flux)	150
Daily magnetic flux index	4
Solar Radiation Pressure Area (A)	10 m <sup>2</sup>
Spacecraft mass (m)	1000 kg

For this simulation, the space-based sensor platform was given a polar Low Earth Orbit described by the initial ECI state vector provided in Table 3.

Table 3: Space-Based Sensor Initial ECI State Vector

Epoch Date (UTC)	x-position (km)	y-position (km)	z-position (km)	x-velocity (km/s)	y-velocity (km/s)	z-velocity (km/s)
01/01/2014 00:00:00	7578.13700	0	0	0	0	7.2525

The initial ECI state vectors of the Geosynchronous Earth Orbit (GEO) targets in which the sensor is tasked to obtain tracks are included in Table 4.

Table 4: GEO Target ECI State Vectors

Epoch Date (UTC)	x-position (km)	y-position (km)	z-position (km)	x-velocity (km/s)	y-velocity (km/s)	z-velocity (km/s)
01/01/2014 00:00:00	42164.00000	0	0	0	3.07467	0
01/01/2014 00:00:00	42163.98395	36.79503	0	-0.00268	3.07467	0
01/01/2014 00:00:00	42163.98395	-36.79503	-36.79501	0.00268	3.07467	0

#### 4. TARGET ILLUMINATION MODEL

For model simplification, all targets are modeled as a Lambertian sphere. The total photon flux (i.e. illumination) of the target is dependent on the waveband of the observing sensor in which to calculate. For the generic space-based optical sensor, the waveband is in the visible spectrum, note that this target illumination model will support other wavebands as well. Also, because the target is in a Geosynchronous Orbit, its distance from Earth's is large enough such that the Earth can be modeled as a Lambertian sphere as well. This simplifies the Earth reflectance models and allows the use of a Lambertian spherical approximation.

The total photon flux,  $\Phi_{\text{tot}}$ , in photons s<sup>-1</sup> m<sup>-2</sup> of a target observed from a sensor can be found in (5):

$$\Phi_{\text{tot}} = \Phi_{\text{TSE}} + \Phi_{\text{ES}} + \Phi_{\text{S}} + \Phi_{\text{TE}} \quad (5)$$

Where  $\Phi_{\text{TSE}}$  is the photon flux from self-emission (thermal) of the target,  $\Phi_{\text{ES}}$  is the photon flux from the Earth shine reflecting on the target,  $\Phi_{\text{S}}$  is the photon flux from the solar reflection on the target, and  $\Phi_{\text{TE}}$  is the photon flux from the thermal radiation reflected from the Earth on the target.

The photon emissivity (P s<sup>-1</sup> m<sup>-2</sup>) from thermal self-emission given a specific sensor waveband can be numerically computed from the Planck function (6) [8].

$$\Phi_{TSE} = \int_{\lambda_{\min}}^{\lambda_{\max}} \frac{c_1 \lambda^{-5}}{\exp(c_2 / \lambda T_{tgt}) - 1} d\lambda \quad (6)$$

Where  $c_1$  and  $c_2$  are constants,  $c_1 = 2\pi h c^2 = 3.74 \times 10^{-16} \text{ Wm}^{-2}$  and  $c_2 = \frac{hc}{k} = 1.44 \times 10^{-2} \text{ m K}$

The temperature,  $T_{tgt}$ , of the target can be approximated using an isothermal uniform satellite temperature model using the conservation of energy equation (7) (i.e. energy emitted is equal to the energy absorbed) [9]:

$$\varepsilon_{tgt} \sigma A_{tgt} T_{tgt}^4 = \varepsilon_{tgt} \sigma A_{tgt} F_{tgt,e} T_e^4 + Q_{sun} + Q_{er} + Q_i \quad (7)$$

Rearranging (7) for the uniform temperature of the target, in steady state, is found from (8):

$$T_{tgt} = \sqrt[4]{F_{tgt,e} T_e^4 + \frac{Q_{sun} + Q_{er} + Q_i}{\varepsilon_{tgt} \sigma A_{tgt}}} \quad (8)$$

Where  $\varepsilon_{tgt}$  is the target emissivity.  $\sigma$  is the Stefan-Boltzman constant.  $T_e$  is the uniform temperature of the Earth.  $Q_i$  is the internally generated power of the target in watts (from averaging the generated power of many active satellites over their spherical area in GEO, assume  $271 \text{ W/m}^2$ ).  $Q_{er}$  is the Earth reflected solar input which can be computed analytically for satellites in GEO as shown in equation (9):

$$Q_{er} = I_{sun} \alpha_E \frac{A_E p(\theta_1)}{\pi d_1^2} (\alpha_{tgt} A_{\perp}) \quad (9)$$

The phase integral function,  $P(\theta)$ , can be described in (10):

$$p(\theta) = \frac{2}{3\pi} ((\pi - \theta) \cos \theta + \sin \theta) \quad (10)$$

$A_{\perp}$  is the target cross section area,  $\alpha_{tgt}$  is its surface absorptivity,  $I_{sun}$  is the total solar intensity value of the sun reaching Earth's surface ( $1366.1 \text{ W/m}^2$  corresponds to the STME E490 2000 Standard),  $d_1$  is the distance from the center of the earth to the target,  $A_E$  is the surface area of the Earth,  $\alpha_E$  is the Earth Albedo, and  $\theta_1$  is the angle between the Earth-Sun and the Earth-target vectors. The solar input to the spacecraft is described by (11).

$$Q_{sun} = \alpha_{tgt} A_{\perp} I_{sun} \quad (11)$$

$F_{tgt,e}$  is the view factor of the Earth from the target and can be computed in (12).

$$F_{tgt,e} = \left( 1 - \sqrt{1 - \frac{R_e^2}{d_1^2}} \right) \frac{1}{2} \quad (12)$$

The photon flux from reflected solar energy from the Earth is described by (13)

$$\Phi_{ES} = I_{\lambda sun} \frac{\alpha_E A_E p(\theta_1)}{\pi d_1^2} \frac{\alpha_{tgt} A_{\perp} p(\theta_2)}{\pi d_2^2} \quad (13)$$

Where  $I_{\lambda sun}$  is the irradiance of the sun given a specific waveband (can be determined from a table lookup given from the 2000 ASTM Standard Extraterrestrial Spectrum).  $d_2$  is the distance from the target to the sensor.  $\theta_2$  is the angle between the two vectors that describe  $d_1$  and  $d_2$  (Earth phase angle on the target). The flux from direct solar illumination can be determined from (14):

$$\Phi_S = I_{\lambda sun} \frac{\alpha_{tgt} A_{\perp} p(\xi)}{\pi d_2^2} \quad (14)$$

Where  $\xi$  is the solar phase angle (angle between the sun-target vector and the target-sensor vector,  $d_2$ ). The photon flux related to the thermal spectrum reflectance of the Earth temperature on the target can be found from (15):

$$\Phi_{TE} = I_{EarthThermal} \frac{\alpha_{tgt} A_{\perp} p(\theta_2)}{\pi d_2^2} \quad (15)$$

Where  $I_{EarthThermal}$  is the computed flux over the sensor waveband using the thermal self-emission in (6).

## 5. SENSOR-TARGET TRACKING CONOPS

The space-based platform must slew to align the sensor boresight vector in the direction of the object it has been tasked to track. Since it is assumed that there is no additional tracking intelligence on-board the sensor payload, consider the scenario where the sensor is commanded to slew to a certain RA/DEC position at a specified time. This is considered a no-track CONOPS as opposed to a sidereal track CONOPS (e.g. where the sensor is tracking the relative star motion) or an object track CONOPS (e.g. where the sensor is tracking the relative motion of the object). This no-track CONOPS appears to be representative of the type of tracking performance one would expect when working with space-based sensors designed for other missions outside of SSA. Tracking opportunities were selected based on predicting the SNR and Probability of detection, Pd, of a target of interest and selecting the opportunities corresponding to the greatest Pd without violating any sensor constraints (i.e. sensor solar exclusion angles, maximum slew rate constraints, etc.)

## 6. SPATIAL/TEMPORAL BACKGROUND AND ANOMALOUS PIXEL CORRECTION

Under certain circumstances, the data obtained from an electro-optical sensor system has sufficient noise such that pre-processing is necessary before running a feature point detection algorithm on the collection data. Under those circumstances, further processing is performed to reduce random noise (e.g. frame stacking, velocity filtering). Some performance tuning may be necessary as this has an associated artifact of further reducing the signal strength. At a very high level, it is possible to combine collection data from different points in time and slightly different pixel positions together and use that knowledge to further clean each individual frame. This process is outlined in Fig 3.

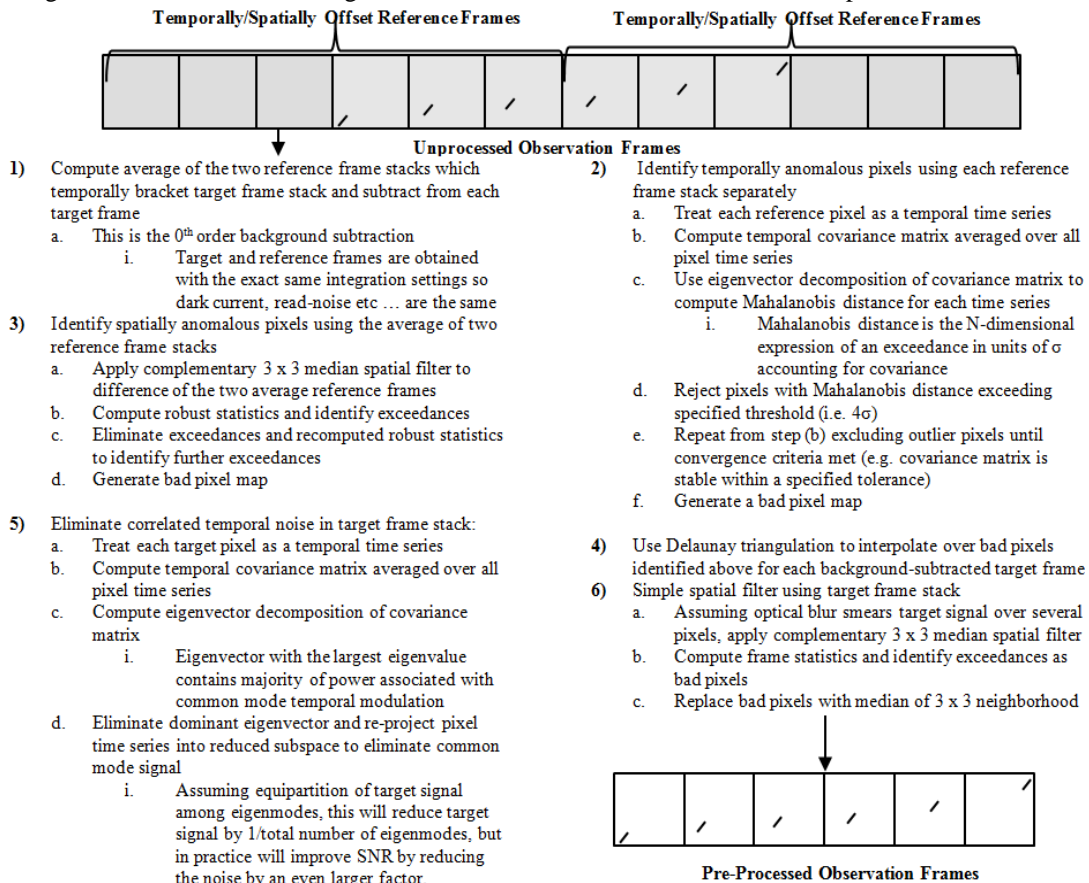


Fig 3: Spatial/Temporal Background & Anomalous Pixel Correction Process



## 7. GEODETICA: RSO DETECTION AND DISCRIMINATION ALGORITHM

Once a set of frames has been suitably pre-processed, space objects are detected and localized within each frame using a segmentation algorithm based on the concept of Phase Congruency followed by a centroid and corner localization procedure. In image processing segmentation is the assignment of image pixels as belonging to either foreground objects or the background. Often in the processing of images from space sensors image segmentations are performed by setting a threshold in image intensity. Global thresholds in intensity cause many undesirable effects due to non-flat noise backgrounds caused by stray light or other artifacts from pre-processing which complicate subsequent RSO localization and discrimination processes. Other algorithms which perform this function also perform segmentation on various additional aspects of image data including segmentation based on motion, signal to noise ratio, and higher order statistical moments. The segmentation based on Phase Congruency used in this paper assigns pixels based on moments of a measure of local energy which is invariant to local image contrast. Additionally, subsequent localization of segmented signals do not suffer the biases typically caused by other local energy segmentation methods due to the implicit Gaussian smoothing used. The Phase Congruency model for feature detection does not assume features are local maxima in the intensity gradient, rather it postulates that features, in this case star and RSO dots and streaks, are located at points in the image where the Fourier components are maximally in phase. The local energy of a signal,  $PC(x)$ , is represented using (16):

$$PC(x) = \frac{|E(x)|}{\sum_n A_n(x)} \quad (16)$$

The standard way of visually conveying this concept is to notice that the Fourier components are all in phase at the location of the step edge in the function shown in Fig 4 shows an additional geometric interpretation of the concept where if the Fourier components are plotted tip to tail as complex vectors, an in phase and therefore perceptible location would achieve a large radius or have a large local energy, while a location which is more like noise would behave like a random walk and not achieve the same value of local energy. In fact this concept can be used to model the behavior of noise in a given sensor and to define thresholds which are directly related to the probability of false alarms.

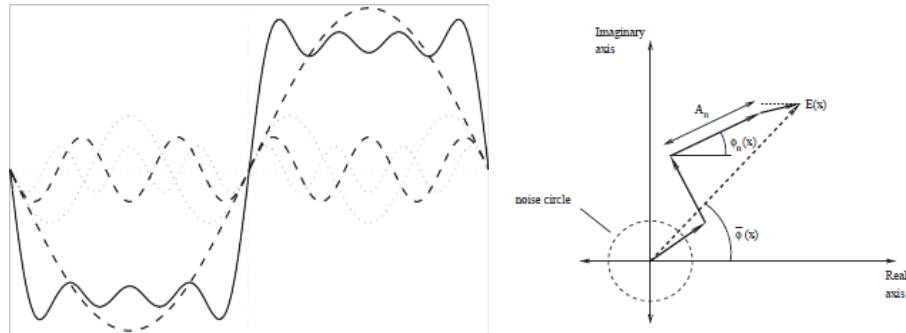


Fig 4 (left) Multiple Fourier Components of a periodic signal in phase at the step edge, (right) Fourier components plotted tip to tail in the polar diagram

The concept of Phase Congruency and its application to imagery for the purposes of finding edges and corners was first developed by Peter Kovesi [10]. In that work he explains that the minimum and maximum moments of this measure can be directly computed and used to define edges and corners. For the work performed in this paper, the corners are used to localize space object centers which are typically co-located with intensity centroids of constant intensity signals, as well as streak endpoints in the case that apparent motion was captured over a single image exposure time. Currently only centroids are associated frame to frame but sufficient information is provided by the corners for additional feature descriptions which can be used for object and motion discrimination. Figure 6 shows the application of this segmentation technique followed by centroiding and corner localization in order to extract a streaking signal from an image with a gradient background. Following the extraction of star and RSO signals in each frame, a nearest neighbor association is performed in order to build the observed track of the RSO and determine the observed right ascension and declination as a function of time. Once these parameters have been determined for all observations, an orbit for the observed RSO can be estimated.

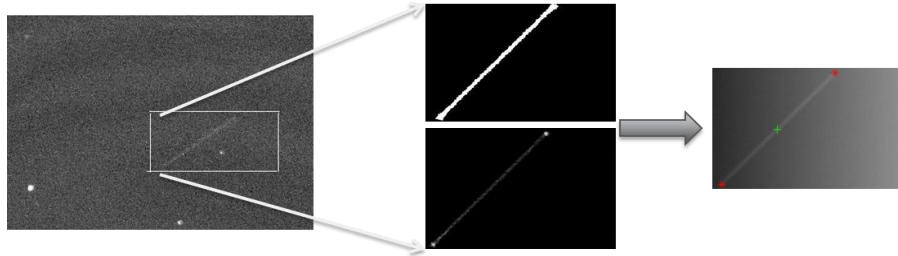


Fig 5: Streaking RSO Segmented Using GEODETICA Including Simultaneous Determination of the Centroid and Endpoints (Note this graphic is simulated sensor data)

## 8. CAR-MHF ORBIT DETERMINATION ALGORITHM

The Constrained Admissible Region Multiple Hypothesis Filter (CAR-MHF) is an optical measurement (i.e. angles-only) initial orbit determination (IOD) strategy that combines the track initialization capability of the CAR (which creates a set of hypothetical trajectory estimates) with an MHF that implements an unscented Kalman filter (UKF), see Stauch et al. for a more detailed discussion [11]. As the name suggests, the CAR involves constraining the possible ambiguity space to an admissible region, following the method presented by Milani [12]. A tracklet of optical data (a set of 3 or more closely-spaced angles-only measurements) can be compressed to form an angles and angle-rates measurement quadruplet (based on the raw measurement noise). As shown by DeMars et al., [13] this measurement can be used to create semi-major axis (SMA) and eccentricity (e) constraints in range/range-rate space, creating a CAR tailored to the type of RSO one might be interested in (i.e. GEO). Even when constrained, the region is likely too large to be used to initiate a single filter, thus a grid can be formed within the CAR to form a set of suitable hypotheses. This yields a set of hypothesis in observation space, which can be passed through an unscented transform [14] to produce a set of hypotheses in Cartesian state space that can readily form the a priori means and covariances for the MHF.

The MHF used in CAR-MHF follows the method introduced by DeMars and Jah [15] in which the estimate of an object is represented by multiple hypotheses. It utilizes the UKF, a special case of the sigma-point Kalman filter (SPKF) [16] that employs the unscented Transform [14]. As opposed to the linear traditional Kalman filter, the full non-linear equations of motion and measurement-state equations are used. Each hypothesis (initialized via CAR) is propagated and updated with a UKF, in parallel. Additionally, a weighting term is carried with each hypothesis. All hypotheses are initially weighted equally and the weights are held constant during the propagation step. During the update step, each hypothesis' weight is updated based on the likelihood that hypothesis originated the observations. Hypotheses may be pruned if and when its weight falls below some desired threshold, allowing the MHF to eventually converge to a single hypothesis.

## 9. RSO DETECTION PERFORMANCE VS SNR FOR NO-TRACK COLLECTIONS

To date it has been observed that this architecture can be used for the detection of both single RSOs as well as multiple RSOs within a collection. Parametric analysis to vary the SNR of the RSO was performed in order to bound the performance of the GOSPA process. Simulation results indicate that an RSO with an SNR above 2 can be effectively detected and discriminated.

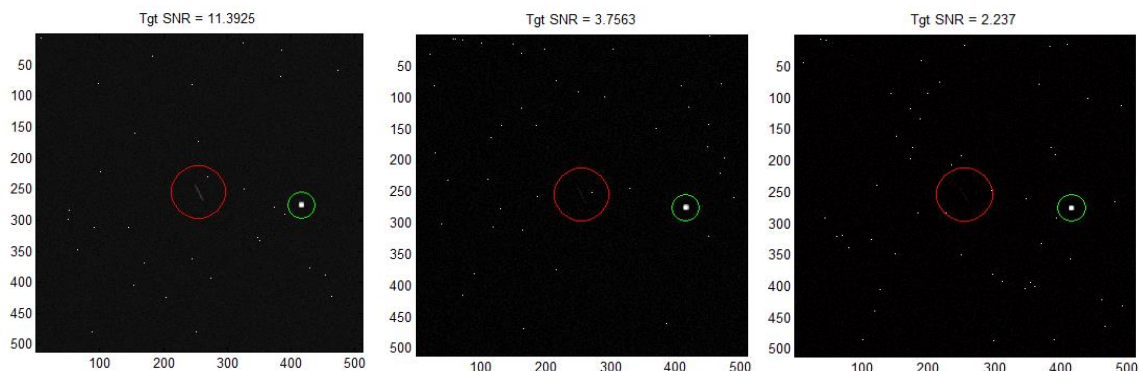


Fig 6: Single RSO Detection Performance (Note this graphic is simulated sensor data)

Empirically, it is easier to automatically identify and track a single RSO using the current implementation of the Feature Point Detection Algorithm at low SNR values than it is to identify and track multiple RSOs at the same SNR. It was found that multiple RSO detections are possible assuming an SNR of 6 or above. The performance of the detection and discrimination architecture is critically associated with the sensor sensitivity, field of view, and other parameters as the algorithms are written to be capable of discerning if the sensor is in a rate track, sidereal track, or other modes which require a minimum number of stars per frame. In cases where the number of RSOs is larger than the observed stars, it can be difficult to distinguish without a catalog this scenario from a rate track. Future work is focusing on enhancing this capability.

## 10. CAR-MHF PERFORMANCE VS POINTING ANGLE UNCERTAINTY

Many low-cost space-based sensor solutions have much larger error in pointing knowledge due to losing lock on stars with a star tracker, IMU drift, and other GN&C limitations. Without the use of star calibration to enhance pointing knowledge, it is still possible to determine a coarse initial orbit of a series of objects using CAR-MHF. For the purposes of this study, CAR-MHF was used to perform an Initial Orbit Determination from a single space-based sensor platform (as described in the previous sections). The RSS position/velocity  $3\text{-}\sigma$  uncertainty associated with each variation of collection cadence was determined for various sensor pointing uncertainties. This should effectively quantify the operational performance of the hypothetical sensor system.

Fig 7 shows the root sum square (RSS) of the position and velocity IOD state vector subtracted from the simulation state vector (truth). Fig 8 displays the ratio of the absolute error in IOD over the  $1\text{-}\sigma$  uncertainty estimates of CAR-MHF. The sensor pointing uncertainty was varied (assuming a Gaussian noise distribution) from 20 – 50 arcsec in both apparent declination and right ascension (28.3-70.7 arcsec RSS). Results show that while it is possible to obtain an IOD on five collections from a single space-based sensor over a 24-hour period, the RA/DEC pointing uncertainty must be at or below 30 arcsec. When the number of collections from a single space-based sensor of the object is sufficiently large (e.g. 10-12 collections/day) there is a point of diminishing returns for both the position and velocity error of the IOD as both states converge to the less than the RA/DEC pointing uncertainty.

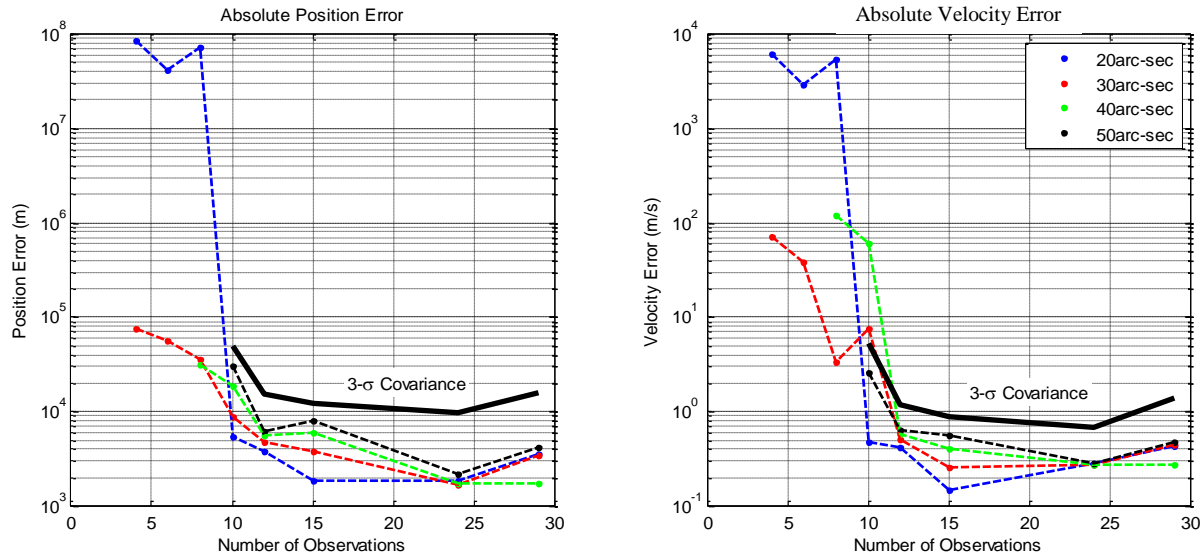


Fig 7: Absolute Position and Velocity Error (Using Truth) of IOD with Variation in Pointing Uncertainty and Number of Collections.  $3\text{-}\sigma$  Position Uncertainty for the 50 arcsec (70.7 arcsec RSS) case overlaid

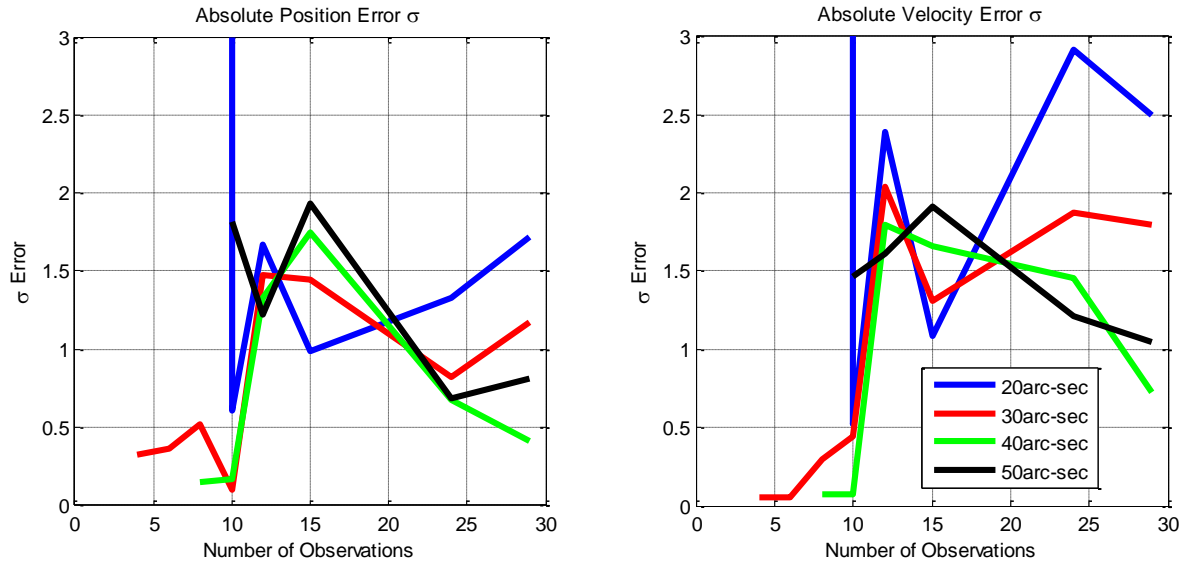


Fig 8: Absolute Error Expressed as  $\#-\sigma$  Uncertainty of IOD with Variation in Sensor Pointing Uncertainty and Total Number of Collections

Note that for all cases where the sensor noise was above 20 arcsec, the absolute error in the state vector estimate falls between 0 and  $3-\sigma$  of the CAR-MHF reported uncertainty estimates. And for all sensor noise cases, the absolute position error is well below the reported  $3-\sigma$  uncertainty for the 50 arcsec sensor noise pointing case. Possible causes of the relatively high error to uncertainty ratios (see Fig 8) for lower sensor noise cases are because of systematic errors induced by the process of extracting the RSO position from the centroiding algorithm (GEODETICA is centroiding on the middle of each streak instead of using one of its end points), simulated discretization of the target on a 7 arcsec/pixel sensor focal plane, different orbit high-precision propagation models (CAR-MHF uses an internal force model with similar but not identical settings to GMAT), and the range/range-rate constraints within CAR do not yet account for angle/angle-rate noise.

## 11. CONCLUSIONS AND FUTURE WORK

This research has demonstrated that, with GOSPA, it is possible to simulate a day in the life of an OrbitOutlook scenario and assess the IOD performance of a sensor system and its CONOPS of looking at a GEO object from LEO. An IOD was obtained with as few as four collections over a 24-hour period. Sensor pointing uncertainties as large as 70.7 arcsec RSS were successfully processed using CAR-MHF. Single RSOs with SNRs above two were properly detected using GEODETICA. GOSPA is a feasible solution when considering a generic low-cost, rapidly deployable, and highly customizable optical signal processing framework for contributing SSA space-based sensor demonstration projects under the OrbitOutlook program. GOSPA was designed around real-world sensor operations which is why it includes support for noisy data (low target SNR) and large uncertainties in sensor pointing knowledge.

With only slight modifications to the space-based platform propagation routine, GOSPA will support ground-based optical sensors. Its capabilities can also be adapted to process and predict the performance of an ad-hoc sensor network based on the previous satellite ephemeris data provided by the Space Surveillance Network (e.g. both IOD and OD). GOSPA could also be used for sensor performance trade studies of ground and space-based optical sensor architectures.

Ongoing improvements are made by AFRL/RV to the feature point detection algorithms in GEODETICA and to CAR-MHF. Since the evaluation of CAR-MHF, another version has been released with updated filters and smoothers which may allow for fewer and noisier observations in order to satisfy conditions for computing an IOD. Work can also be performed to provide support for handling RADAR and passive-RF collectors within GOSPA. This would involve adding a CAR-MHF feature to allow for the processing of range and range-rate information when it is available. The systematic errors observed in the CAR-MHF Performance vs Pointing Angle Uncertainty section can be further reduced by calibrating satellite force models, using a smaller sensor detector IFoVs, and experimenting with GEODETICA streak end-point detection vs centroiding routines in the image processing portion of GOSPA.

## 12. REFERENCES

- 
- [1] Blake T., *ORBIT OUTLOOK*, DARPA Tactical Technology Office, Arlington, Virginia, 2014.
- [2] *Space Acquisitions Development and Oversight Challenges in Delivering Improved Space Situational Awareness Capabilities*. Rep. Government Accountability Office, 27 May 2011.
- [3] Sharma, J. et al, Improving Space Surveillance with Space-Based Visible Sensor, MIT Lincoln Laboratory, 2001.
- [4] Cohn S. and Lomheim T.S., “Flow Down of Sensor Chip Assembly (SCA) Requirements for A Low Background Space Tracking Application,” M.S.S. Technology Specialty Group, The Aerospace Corporation, February, 2003.
- [5] Lomheim T. et al, “Performance/Sizing of an Infrared Scanning Point-Source Sensor,” Aerospace Conference, 1999. Proceedings. 1999 IEEE, Publication Date: 1999, Volume: 4, On page(s): 113-138 vol.4.
- [6] Tobin, S. et al, “1/f Noise in (Hg,Cd) Te Photodiodes,” IEEE Transactions on Electronic Devices, Vol. ED-27, No. 1, January, 1980.
- [7] General Mission Analysis Tool (GMAT) Mathematical Specifications DRAFT. NASA Goddard Space Flight Center. 07/25/2013.
- [8] Lynch P., Section 4.2: Blackbody Radiation Slides, <http://maths.ucd.ie/met/msc/fezzik/PhysMet/>. Meteorology and Climate Centre. 2004.
- [9] Griffin M. and French J., Space Vehicle Design. Second Edition. AIAA. 2004.
- [10] Kovesi P.D., : Image features from phase congruency. *Videre: Journal of Computer Vision Research* 1 (1999) 1–26 <http://mitpress.mit.edu/e-journals/Videre/>.
- [11] Stauch J. Baldwin J. Jah M.K. Kelecy T. and Hill K., “Mutual Application of Joint Probabilistic Data Association, Filtering, and Smoothing Techniques for Robust Multi-Sensor/Space-Object Tracking”, pending publication, AIAA Space and Astronautics Forum and Exposition: AIAA/AAS Astrodynamics Specialist Conference, San Diego, CA, Aug. 2014.
- [12] Milani, A. Gronchi G.F. Vitturi M. and Knezevic Z., “Orbit determination with very short arcs. I admissible regions,” *Celestial Mechanics and Dynamical Astronomy*, vol. 90, pp. 59–87, July 2004.
- [13] DeMars K. J. and Jah M.K., “Probabilistic initial orbit determination using gaussian mixture models,” *Journal of Guidance, Control, and Dynamics*, vol. 36, no. 5, pp. 1324–1335, 2013.
- [14] Julier S. J. and Uhlmann J. K., “Unscented filtering and nonlinear estimation,” *Proceedings of the IEEE*, vol. 93, March 2004.
- [15] DeMars K.J, Jah M.K. and Schumacher P.W. , “Initial orbit determination using short-arc angle and angle rate data,” *IEEE Transactions on Aerospace and Electronic Systems*, vol. 48, no. 3, pp. 2628–2637, 2012.
- [16] Julier S. J. Uhlmann J.K. and Durrant-Whyte H.F., “A new method for the nonlinear transformation of means and covariances in filters and estimators,” *IEEE Transactions on Automatic Control*, vol. 45, pp. 477–482, March 2000.

The views expressed are those of the author(s) and do not reflect the official policy or position of the Department of Defense or the U.S. Government